Manuscript prepared for Atmos. Chem. Phys. Discuss.
with version 1.3 of the LaTeX class copernicus_discussions.cls.
Date: 5 December 2008

Accurate satellite-derived estimates of tropospheric ozone radiative forcing

Joanna Joiner[1], Mark R. Schoeberl[1], Alexander P. Vasilkov[2], Lazaros Oreopoulos[1], Steven Platnick[1], Nathaniel J. Livesey[3], and Pieternel F. Levelt[4]

[1]NASA Goddard Space Flight Center, Greenbelt, MD USA
[2]Science Systems and Applications Inc., Lanham, MD,USA
[3]Jet Propulsion Laboratory, Pasadena, CA, USA
[4]Royal Netherlands Meteorological Institute (KNMI), de Bilt, The Netherlands

Correspondence to: Joanna Joiner
(Joanna.Joiner@nasa.gov)

Abstract

Estimates of the radiative forcing due to anthropogenically-produced tropospheric O_3 are derived primarily from models. Here, we use tropospheric ozone and cloud data from several instruments in the A-train constellation of satellites as well as information from the GEOS-5 Data Assimilation System to accurately estimate the instantaneous radiative forcing from tropospheric O_3 for January and July 2005. We improve upon previous estimates of tropospheric ozone mixing ratios from a residual approach using the NASA Earth Observing System (EOS) Aura Ozone Monitoring Instrument (OMI) and Microwave Limb Sounder (MLS) by incorporating cloud pressure information from OMI. Since we cannot distinguish between natural and anthropogenic sources with the satellite data, our estimates reflect the total forcing due to tropospheric O_3. We focus specifically on the magnitude and spatial structure of the cloud effect on both the short- and long-wave radiative forcing. The estimates presented here can be used to validate present day O_3 radiative forcing produced by models.

1 Introduction

Tropospheric ozone contributes to the greenhouse effect by absorbing in the thermal infrared, primarily in the 9.6μm band. In addition, ozone absorbs sunlight in the visible Chappuis band between 400 and 700 nm and in the ultraviolet Hartley and Huggins bands shortward of about 340 nm. According to estimates in Forster et al. (2007), tropospheric ozone ranks as the third most important anthropogenically-produced gas in terms of climate impact through its direct radiative effects.

Due to the paucity of tropospheric ozone observations over the industrial era, estimates of the radiative forcing caused by changes in tropospheric ozone have been based primarily on results from chemistry transport models (CTMs) with coupled stratospheric and tropospheric chemistry and general circulation models (GCMs) with on-line chemistry (e.g., Gauss et al., 2006). In these models, the anthropogenic contribution

to the tropospheric ozone burden is driven by changes in the emissions of precursors including NO_x, CO, CH_4, and other volatile organic compounds (VOCs), and changes in transport across the tropopause resulting from changes in stratospheric ozone and climate change.

Clouds significantly affect the magnitude and spatial distribution of the tropospheric O_3 radiative forcing, generally decreasing it by 20-60% depending on location (Forster et al., 1996). In the long-wave, clouds decrease the tropospheric ozone radiative forcing at the tropopause. However, in the short-wave, clouds enhance the solar photon pathlength and thus increase tropospheric ozone radiative forcing at the tropopause.

The various satellites in the A-train afternoon constellation provides a wealth of new data that can be used to accurately compute the impact of tropospheric ozone on the local and global radiation budget. In this paper, we use several datasets from A-train satellites to compute daily gridded instantaneous radiative forcing (RF) due to tropospheric O_3. These satellites fly in an afternoon orbit with an ascending equator crossing time of 13:30. Tropospheric ozone is derived from a residual approach that combines information from the Ozone Monitoring Instrument (OMI) and Microwave Limb Sounder (MLS) flying on the National Aeronautics and Space Administration (NASA) Earth Observing System (EOS) Aura satellite building on the work of Ziemke et al. (2006) and Schoeberl et al. (2007). We use cloud properties from the NASA EOS Aqua Moderate Resolution Imaging Spectroradiometer (MODIS) and OMI.

With nearly coincident datasets of cloud properties and tropospheric ozone, we compute the tropospheric O_3 radiative forcing on a daily near-global basis at relatively high spatial resolution. The use of these data sets results in improved estimates of tropospheric O_3 radiative forcing as compared with previous studies. We specifically isolate the impact of clouds separately on the long- and short-wave. We also examine spatial and temporal variations in the sensitivity of the RF to a given change in tropospheric O_3 mixing ratio.

The organization of the paper is as follows: Section 2 and the appendices describe the radiative transfer calculations and input data sets in detail. Results of radiative

forcing calculations are presented in section 3. Section 4 discusses our results in the context of model-generated anthropogenic radiative forcing estimates that provide the basis for magnitudes and uncertainties reported by the Intergovernmental Panel for Climate Change (IPCC). Conclusions are given in section 5.

2 Algorithms and datasets used in radiative transfer calculations

2.1 Radiative transfer calculation

The radiative transfer calculations are performed using stand-alone versions of algorithms developed by Chou and Suarez (1994, 2002, 2003) (henceforth referred to as CS). These algorithms are part of the Goddard Earth Observing System 5 Data Assimilation System (GEOS-5 DAS) (Rienecker et al., 2007) and have been used in previous versions of the GEOS-DAS and other models in the Goddard Laboratory for Atmospheres. Separate algorithms were developed for long-wave (LW) and short-wave (SW) components. Appendix A gives a detailed description of the algorithm.

2.2 Tropospheric ozone mixing ratio from OMI/MLS

The tropospheric column-mean mixing ratio is estimated using a residual method with retrievals of total and stratospheric column ozone from OMI and MLS, respectively, using a slightly modified version of the algorithm developed by Schoeberl et al. (2007). OMI is a nadir-viewing radiometer that measures the solar irradiance and Earth backscattered radiance from 270-500 nm with a spectral resolution of approximately 0.5 nm (Levelt et al., 2006). It provides near-global coverage with a nadir pixel size of 13 $\times$ 24 km in the UV-2 channel used to retrieved total column ozone.

The OMI total column ozone is from collection 3 and is derived using an algorithm similar to the Total Ozone Mapping Spectrometer (TOMS) version 8 (known as OMTO3 version 8.5) (Bhartia and Wellemeyer, 2002). This is one of two OMI total

column O_3 products; The other uses a Differential Optical Absorption Spectroscopy (DOAS). McPeters et al. (2008) and Kroon et al. (2008a,b) discuss the validation of these OMI total ozone data sets. There has been no significant drift in the OMI total columns as compared with the ground-based network of Dobson and Brewer instruments (McPeters et al., 2008). The systematic difference between OMTO3 and ground-based data increased slightly from collection 2 (0.26%) to 3 (-1.3%) (G. Labow, private communication).

One major change in OMTO3 subsequent to these publications is the incorporation of optical centroid cloud pressures (OCCPs) from the OMI rotational-Raman cloud product (OMCLDRR) of Joiner and Vasilkov (2006). The OMI cloud pressures replace a climatology of cloud-top pressures derived from thermal infrared measurements. This change eliminated significant errors in the total column ozone in the presence of bright clouds identified by Joiner et al. (2006) and lessened cloud-induced noise in the retrieved total column ozone similar to the results of Vasilkov et al. (2004). It also reduced differences between the OMI DOAS and OMI TOMS total columns that were noted by Kroon et al. (2008b).

MLS makes millimeter and submillimeter observations by scanning through the atmospheric limb. We use stratospheric column ozone from MLS version 2.2 that has been validated by Froidevaux et al. (2008), Livesey et al. (2008), and Petropavlovskikh et al. (2008). The stratospheric columns from version 2.2 are in better agreement with correlative data sets than version 1.5 (e.g., Petropavlovskikh et al., 2008) with MLS slightly higher than SAGE II ($\sim$1%) in the lower stratosphere (Froidevaux et al., 2008).

Because MLS makes measurements along the Aura orbital track within a narrow swath, its retrievals must be interpolated between orbits to provide daily global estimates of the stratospheric column ozone. Here, MLS ozone profile data between 10 and 215 hPa are spread with a trajectory model as in Schoeberl et al. (2007). The stratospheric column ozone derived from this method is then subtracted from the retrieved OMI total column ozone to yield estimates of the tropospheric column ozone.

Schoeberl et al. (2007) compared a previous version of the OMI/MLS column ozone

between 200 hPa and the surface with ozone sonde data. In the tropics, the mean difference was 2.4 Dobson Units (DU) (sonde higher) with a standard deviation of approximately 5 DU. The differences were larger at middle latitudes with OMI/MLS consistently lower than the ozonesondes by 1-7 DU depending on the season. Standard deviations at mid-latitudes were also higher with values between about 9 and 13 DU also dependent on season.

We have improved the residual approach of Schoeberl et al. (2007) by reducing the influence of *a priori* information in cloudy conditions. In cloudy situations, a portion of the O_3 column beneath the clouds is hidden from the satellite. An estimate of this hidden amount (i.e.the *a priori* information, also commonly referred to as the ghost column) based on climatology is added to the measured column to provide an estimate of the total column. To compute the column-mean volume mixing ratio, $\overline{\chi}$, we use the column measured by OMI, Ω_{meas}, rather than the estimated total column ozone that includes an assumed amount of ozone in the hidden column. Note that the sensitivity of OMI observations to tropospheric O_3 varies with pressure due to both cloud shielding and Rayleigh scattering.

The O_3 column, Ω, in DU between any two pressure levels is given by

$$\Omega = 0.789 \int_{P_{\mathsf{top}}}^{P_{\mathsf{bottom}}} \chi dP, \tag{1}$$

(e.g., Dessler , 2005), where χ is the O_3 volume mixing ratio in units ppmv, and P_{top} and P_{bottom} are the top and bottom pressure levels in hPa. In this work, we define $\overline{\chi}$ as the column-mean mixing ratio corresponding to a broad homogeneous tropospheric layer that produces the observed tropospheric column. We next develop the concept of an effective layer represented by $\overline{\chi}$. The top of this layer is the tropopause, and we define the lower pressure boundary to be P_{eff}. Then, eq. 1 can be rewritten as

$$\overline{\chi} = 1/0.789(\Omega_{\mathsf{meas}} - \Omega_{\mathsf{strat}})/(P_{\mathsf{eff}} - P_{\mathsf{trop}}), \tag{2}$$

where P_{trop} is the tropopause pressure (in hPa) and Ω_{strat} is the stratospheric column ozone.

A first order estimate of P_{eff} can be obtained using the concepts of radiative cloud fraction (f) and optical centroid cloud pressure (OCCP or P_{cld}). f is defined as the fraction of total pixel radiance contributed by the cloudy portion of the pixel. P_{cld} is the pressure of a Lambertian surface with equivalent reflectivity of 80% that produces the observed amount of rotational-Raman scattering for a given f. The accuracy of this Mixed Lambertian model has been examined in detail by Vasilkov et al. (2008).

The measured portion of the tropospheric column, Ω_{trop}, is defined as $\Omega_{\text{meas}} - \Omega_{\text{strat}}$. Then, Ω_{trop} can be written as

$$\Omega_{\text{trop}} = 0.789[(1-f)\chi_{\text{clr}}(P_{\text{surf}} - P_{\text{trop}}) + f\chi_{\text{cld}}(P_{\text{cld}} - P_{\text{trop}})], \tag{3}$$

where χ_{clr} and χ_{cld} are the column-mean mixing ratios for layers between the tropopause and either the surface or P_{cld}, respectively. Setting $\chi_{\text{clr}} = \chi_{\text{cld}} = \overline{\chi}$, (3) can be rewritten as

$$\Omega_{\text{trop}} = 0.789[\overline{\chi}(P_{\text{eff}} - P_{\text{trop}})], \tag{4}$$

where

$$P_{\text{eff}} = (1-f)P_{\text{surf}} + fP_{\text{cld}}. \tag{5}$$

The computation of $\overline{\chi}$ with this approach reduces noticeable cloud-induced artifacts in the column-mean mixing ratio. As a result, pixels with high cloud amounts are no longer discarded. The agreement between satellite-derived and sonde-based tropospheric column ozone is significantly improved. For example, the overall correlation coefficient between sonde and satellite 200hPa to surface column increased from ~0.5-0.7 to ~0.8. Note that for bright pixels ($f = 1$), $\overline{\chi}$ can be computed accurately and represents the column-mean mixing ratio between the tropopause and the optical centroid cloud pressure, P_{cld}. This is precisely the quantity that is needed for RF calculations in the short-wave.

The specification of the tropopause affects our radiative forcing calculation in two ways. Firstly, the selection of a particular tropopause definition determines the amount

of ozone assigned to the troposphere and thus the derived column-mean mixing ratio from the residual method. Secondly, it determines how much of the atmosphere is included in the RF calculation. This particularly affects the calculation of long-wave RF because of high sensitivity to ozone near the tropopause.

In this work, we will apply two definitions of the tropopause height. The first is the standard lapse rate definition (the lowest level at which the lapse rate decreases to 2K/km or less provided that the average lapse rate between this level and all higher levels within 2 km does not exceed 2K/km). The second method relies primarily on a dynamic definition and uses the lowest altitude corresponding to 3.5 PVU (Potential Vorticity Units), the 380K surface, the cold point, or the lapse rate definition. The PV tropopause definition is usually lowest in altitude outside the tropics.

Figure 1 shows examples of the derived daily column-mean mixing ratio, $\overline{\chi}$, from OMI/MLS derived with the lapse-rate tropopause definition. Figure 2 similarly shows monthly mean fields of $\overline{\chi}$. Tropospheric ozone has significant spatial variations on both daily and seasonal time scales. In the remote tropical Pacific, areas of deep convection (high values of cloud fraction and optical thickness) correspond to low O_3 mixing ratios shown in figure 1. The reported mixing ratios in the presence of bright clouds represent that inside the upper portions of the clouds (Ziemke et al., 2008). The low mixing ratios can result from ozone-poor boundary layer air that is lifted into the upper troposphere (Kley et al., 1996; Folkins et al., 2002; Solomon et al., 2005).

Similar to Schoeberl et al. (2007), we filter out suspect data. Data are not used when the tropopause is at a pressure greater than 320 hPa, primarily to minimize excessive extrapolation of MLS data (only used down to 215 hPa). Data are also discarded when the derived tropospheric column amount is greater than 120 DU. This can occur when the tropopause pressure is ill-defined or may indicate situations where the trajectory approach is suspect. When the derived value of $\overline{\chi}$ is less than zero, it is set equal to zero. OMI cloud pressures are currently not used to derive column ozone over snow and ice. Therefore, the column-mean mixing ratio may be underestimated over snow and ice when optically thick clouds are present. Note also that there are no OMI data

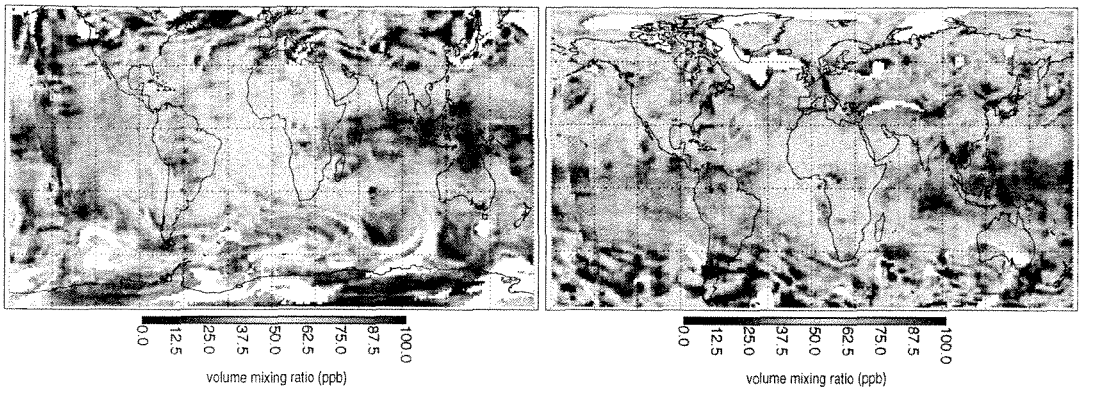

Fig. 1. Column-mean O_3 tropospheric mixing ratio derived from OMI/MLS for 01 January (left) and 01 July 2005 (right). Missing values (white areas) occur where either no data are available or where quality control checks flag the data as suspect (see text).

in the polar night.

2.3 Cloud parameters from MODIS

We use estimates of cloud optical thickness, effective radius, and phase from MODIS daily gridded $1^\circ \times 1^\circ$ level 3 (L3) data sets (Platnick et al., 2003). The dataset includes gridpoint means and histograms of cloud optical depth separately for ice and water clouds. We also use the associated cloud fractions for ice and water clouds. These are the fractions of successful cloudy retrievals with respect to all successful retrievals within a gridbox. Note that MODIS cloud optical thicknesses have an upper limit of $\sim$100. This has a minimal impact on our short-wave RF calculations, because cloud reflectance and transmittance are effectively saturated at this value. Lastly, we use mean daytime cloud-top pressures. These are derived from either the CO_2 slicing

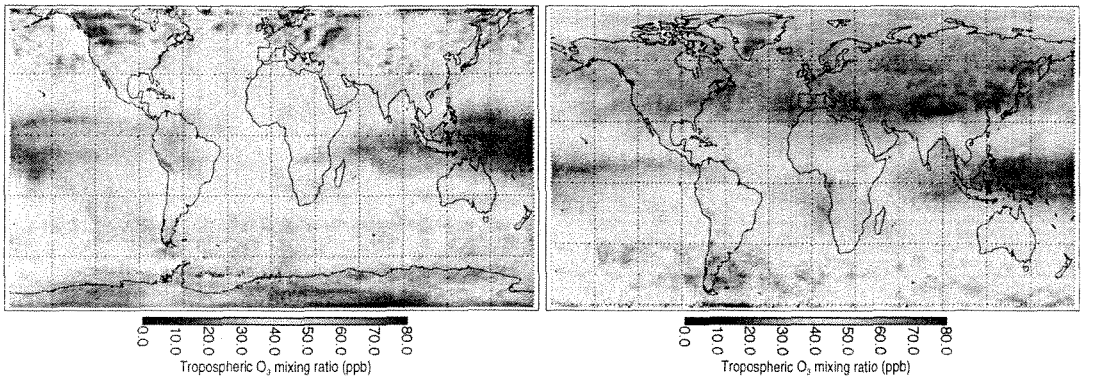

Fig. 2. Monthly average column-mean tropospheric O_3 mixing ratio for January (left) and July (right) 2005.

approach of Menzel et al. (1992) or from the infrared 11μm window channel brightness temperature as described in Platnick et al. (2003).

2.4 Optical centroid cloud pressure (OCCP) from OMI

Significant differences exist between cloud-top pressures derived from thermal infrared measurements and optical centroid cloud pressures (OCCP) derived from photon-path-type measurements. OCCP can be derived from a variety of techniques including oxygen A-band absorption (e.g., Rozanov et al., 2004), oxygen dimer absorption (e.g., Sneep et al., 2008), and rotational-Raman scattering (e.g., Joiner et al., 2004). The latter two have been utilized with OMI. Vasilkov et al. (2008) showed that the derived OCCPs were consistent with simulations that used optical depth profiles derived from a combination of CloudSat radar reflectivity profiles (Stephens et al., 2002) and MODIS cloud optical depths.

Ziemke et al. (2008) have shown that the large differences between MODIS cloud-top pressures and OMI OCCPs in convective clouds are due in part to the fact that clouds are vertically inhomogeneous. CloudSat/MODIS retrievals show that tropical deep convective clouds are relatively thin near the top with cloud extinctions peaking between ~400 and 600 hPa. By computing ozone Jacobians within convective clouds, Ziemke et al. (2008) demonstrate that photons penetrate significantly inside these clouds, reaching pressures near the OCCP with enhanced absorption due to multiple scattering in the upper portions of the clouds. They further demonstrated that the concept of the OCCP can be used to estimate O_3 absorption inside clouds with good accuracy. Therefore, the OCCP is more appropriate than the cloud-top pressure for RF calculations in the short-wave.

Here we use OCCPs from the OMI rotational-Raman algorithm (Joiner and Vasilkov, 2006). Figure 3 shows a sample day of retrieved OCCP. Over ocean the OCCPs are general large (low altitude clouds), except in regions of tropical deep convection and frontal convection in the extra-tropics. The difference between the OMI OCCP and the MODIS cloud-top pressure is also shown in figure 3. The largest differences are found in conjunction with deep or frontal convection, especially around the edges of the convection where outflow produces thin cirrus above lower level water clouds. Vasilkov et al. (2008) showed that in such situations when the upper cirrus deck has an optical thickness of ~10 or less, the OCCP should be close to the top of the lower cloud deck.

The OCCP is almost always greater than the cloud top pressure. However, the optical centroid pressure may be less than the cloud top pressure due to changes in clouds that occur between the Aqua and Aura overpasses (at this time, the difference was ~15 minutes). Errors in either the MODIS or OMI cloud pressures may also produce this type of difference. UV-absorbing aerosol (e.g., dust or smoke) above or embedded within clouds can erroneously reduce the retrieved OMI cloud fractions and pressures (Vasilkov et al., 2008). MODIS cloud pressures derived from the window brightness temperature technique are also prone to errors when there are temperature inversions or when cloud emissivity is less than unity.

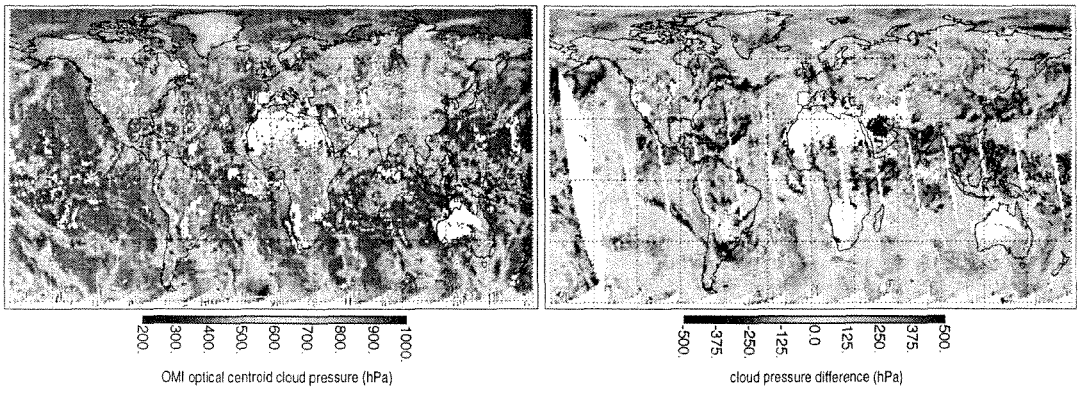

Fig. 3. Gridbox mean optical centroid cloud pressure (OCCP) from OMI (left) and OCCP minus MODIS cloud-top pressure (right) for 01 July 2005.

2.5 Meteorological parameters from the GEOS-5 data assimilation system

Atmospheric profiles of temperature, water vapor, and stratospheric ozone are taken from the Goddard Earth Observing System 5 Data Assimilation System (GEOS-5 DAS) (Rienecker et al., 2007). The GEOS-5 DAS is run at a horizontal resolution of $0.5° \times 0.625°$. The analysis system uses the Gridpoint Statistical Interpolation (GSI) scheme developed at the National Oceanic and Atmospheric Administration (NOAA) National Centers for Environmental Prediction (NCEP) that is part of their operational global weather prediction system.

The system ingests satellite data from operational meteorological satellites including microwave and infrared radiance data from the TIROS Operational Vertical Sounder (TOVS), and the NASA Aqua Atmospheric InfraRed Sounder (AIRS) and Advanced Microwave Sounding Unit A (AMSU-A). These data provide information about the global temperature and humidity fields. Stratospheric O_3 distributions are constrained by the

assimilation of Satellite Backscatter UltraViolet 2 (SBUV-2) spectrometer retrievals. Stratospheric O_3 impacts our calculations of the tropospheric O_3 radiative forcing in that it affects the downwelling flux at the tropopause.

2.6 Surface albedos and emissivity

In the short-wave, the CS code accepts spectrally constant albedos for direct and diffuse fluxes in the UV/Visible region. Here, we use 16-day gridded albedos from the MODIS filled-land surface albedo product (MOD43B3) (Lucht et al., 2000). Separate values are provided for white and black skies. The former (latter) are used for calculations in cloudy (clear) skies.

Over ocean, we use a model of the surface albedo from Jin et al. (2004). The albedo varies with surface wind speed. Therefore, we use estimates of the 2m wind speed from the GEOS-5 DAS. We interpolate the albedos to 600 nm, the approximate peak of the Chappuis O_3 band. We use the Near Real-Time SSM/I EASE-Grid Daily Global Ice Concentration and Snow Extent (NISE) data set (Nolin et al., 1998) to identify gridboxes containing sea ice. If sea ice is identified and the MODIS albedo product does not provide an appropriate value, we use the 380 nm reflectivity from a TOMS monthly climatology (C. Ahn, private communication).

In the thermal infrared, we use an annual average surface emissivity database at $1^\circ \times 1^\circ$ resolution compiled from Wilber et al. (1999). Here, we interpolate the spectral surface emissivity to a wavelength of 9.6μm where O_3 absorption is at a maximum.

3 Results

The tropospheric O_3 RF shown here is computed at the tropopause and is instantaneous, i.e., not dynamically adjusted as in Forster et al. (2007) to allow stratospheric temperatures to readjust to radiative equilibrium. The adjustment produces a decrease of between 8 and 20% as compared with instantaneous values (e.g., Hauglustaine et

al., 2001; Berntsen et al., 1997; Haywood et al., 1998). It is not possible to disentangle the anthropogenic contribution to the tropospheric O_3 column from that produced in nature with our satellite-derived data set. Therefore, we define the tropospheric O_3 perturbation as the satellite-derived column-mean mixing ratio distributed uniformly in the vertical (i.e., the reference is with respect to zero tropospheric ozone). No distinction is made between anthropogenically-produced O_3 and stratospheric O_3 transported across the tropopause in fold regions (as seen in figure 1). Our results thus represent an upper bound on the RF due to anthropogenically-produced tropospheric ozone. While our definition of tropospheric O_3 RF is inconsistent with that of Forster et al. (2007), it is relatively straight-forward to compare present day model-generated tropospheric O_3 (anthropogenic + natural) RF with our satellite-derived results.

To derive $\overline{\chi}$ and in the following radiative calculations, we have assumed that the mixing ratio is constant throughout the tropospheric column. Kiehl et al. (1999) used a constant mixing ratio perturbation in their radiative forcing calculations and found it to be a reasonable approximation of differences between ozonesonde data obtained in polluted and clean conditions. Kiehl et al. (1999) further examined the sensitivity of radiative forcing to this choice and found that it changed by $\pm$ 15% when they instead used perturbations with a constant slope in mixing ratio as a function of altitude.

For short-wave calculations, we compute the diurnally-averaged RF. Because it is important to use the column-mean tropospheric mixing ratio coincident with the cloud property retrievals to compute the RF, particularly in convective regions, we assume that the MODIS Aqua daytime cloud properties and the column-mean O_3 mixing ratios persist throughout day. We then perform calculations every two hours at the appropriate solar zenith angle. We compared our two hour averages with one hour averages and found negligible differences on a global daily average.

For LW calculations, we average the RF computed using GEOS-DAS data at the synoptic time closest to the A-train 1:30 and 13:30 overpasses. In this way, we capture to a large degree the high and low extremes of the surface skin temperature. As in the short-wave calculations, we leave the cloud properties and tropospheric O_3 fixed at the

Aqua MODIS 13:30 values.

Details regarding the use of the MODIS and OMI retrieved cloud parameters are given in Appendix B1-B2 along with sensitivity studies. Similarly, the sensitivity of the LW and SW RF to the tropopause definition is explored in Appendix B3. All results shown here use the common lapse-rate tropopause definition for computing both the tropospheric O_3 mixing ratio and the RF.

3.1 Daily long- and short-wave RF

Figure 4 shows the LW and SW total-sky tropospheric O_3 RF for 01 July 2005 and the impact of clouds (total- minus clear-sky tropospheric O_3 RF). High values occur over the Sahara and the middle East, as noted in previous works, and are understood to occur because of the high surface skin temperatures during the day coupled with low humidity and low cloud amounts and a build up of ozone in the upper troposphere as discussed by Li et al. (2001). The lowest values occur, as expected, in the presence of high clouds (e.g., areas of tropical deep convection). The cloud effect is primarily to reduce the LW RF. However, in a few areas with low clouds and temperature inversions, clouds can increase the LW RF. Examples of this situation include areas off the western coasts of North America and southern Africa as well as in the Arctic. High values of SW RF are concentrated in the northern hemisphere as a result of the larger amount of solar irradiance and tropospheric ozone and primarily occur over clouds or high albedo surfaces such as Greenland and the Sahara.

3.2 Monthly-mean long-wave RF

Figure 5 shows the gridded monthly-mean total-sky LW tropospheric O_3 RF for January and July 2005 effect of clouds. Most of the fine spatial features seen in the daily RF have been smoothed out in the monthly mean. In the winter hemisphere, where surface temperatures are cold over land, the LW RF is small and the effect of clouds is generally small or even slightly positive. Over oceans, where surface temperatures

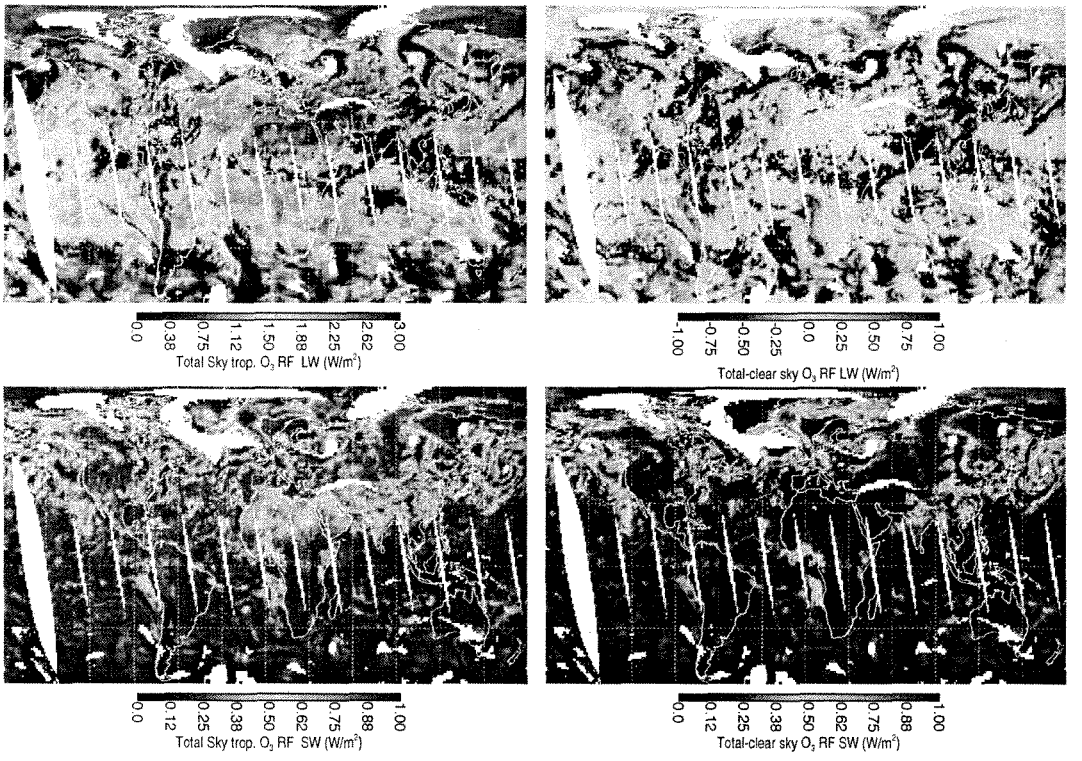

Fig. 4. Instantaneous (unadjusted) daily-averaged total-sky tropospheric O_3 RF: Long-wave (top left) and short-wave (bottom left); Total minus clear-sky RF: Long-wave (top right) and short-wave (bottom right) on 01 July 2005.

can be warmer such as in the gulf stream, clouds can significantly reduce the LW RF. However, in the summer hemisphere, land surface temperatures can be quite warm,

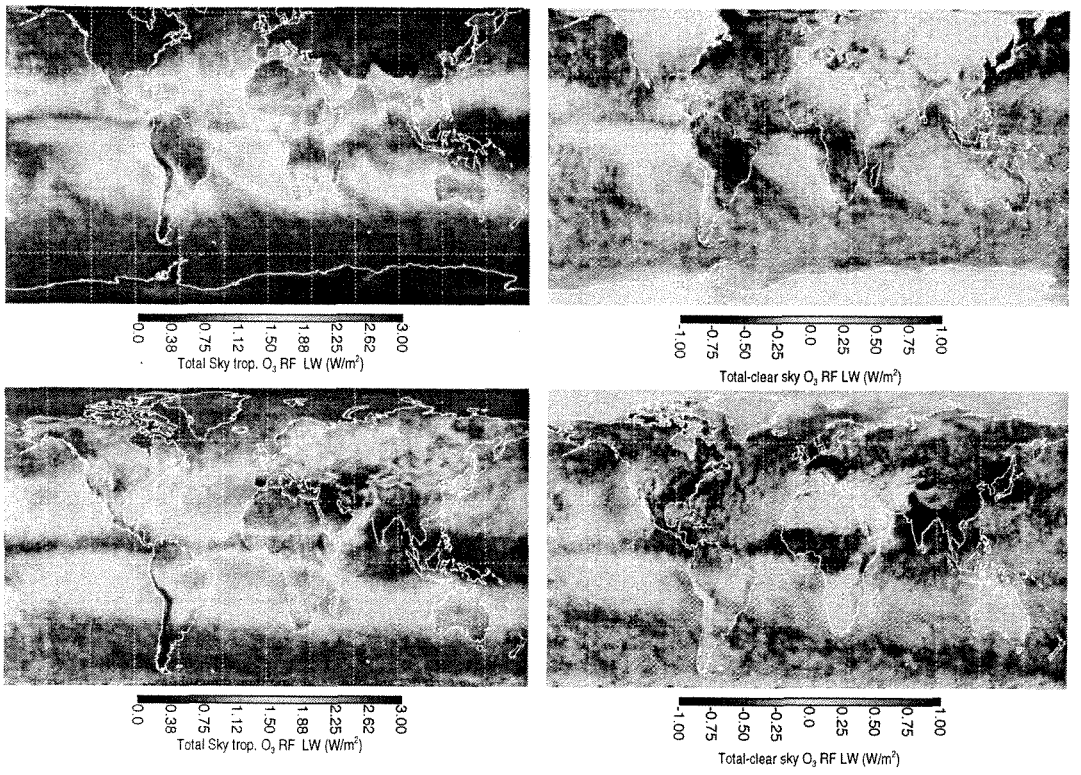

Fig. 5. Total-sky long-wave (LW) tropospheric O_3 RF in 2005: January (top left) and July (bottom left); Total minus clear-sky LW RF: January (top right) and July (bottom right).

giving rise to large RF in the absence of clouds and a large impact of clouds when present (e.g., over India).

Figure 6 shows the total-sky sensitivity of LW RF (in mW/m^2 per ppb change in the

column-mean O_3 mixing ratio) for January and July 2005. The computed LW RF bears a close resemblance to this sensitivity, with a few exceptions. The RF is low over substantial areas in the Pacific, while the sensitivity there is not always small. This is primarily due to low O_3 mixing ratios that result from the lofting of ozone-poor boundary layer air that occurs during convection and outflow. These low mixing ratios can persist for some time so that even when the sensitivity is relatively high, the RF remains low.

Portmann et al. (1997) computed a sensitivity in terms of column amount rather than mixing ratio for clear skies. They showed that for several tropical locations that the forcing was relatively constant (to within $\sim 20\%$) throughout the year. Here, we show that clouds significantly affect the sensitivity both spatially and temporally. Our results show reasonable agreement with those presented in Berntsen et al. (1997) especially considering that the horizontal resolution of their CTM was relatively low ($8° \times 10°$). As expected, our satellite-based estimates show finer spatial structures. However, even after accounting for the fact that their sensitivity was computed with stratospheric adjustment, our global mean values are higher: 34 mW/m^2/ppb as compared with their 20 mW/m^2/ppb and similar values reported in Hauglustaine et al. (2001).

3.3 Monthly-mean short-wave RF

Figure 7 shows the SW RF and cloud effects for January and July 2005. The highest values of SW RF in the northern hemisphere at this time of year occur over southeast Asia. These high amounts of SW RF are primarily due to clouds. In order to obtain these high values, the clouds must be persistent and bright. MODIS data show that the effective radii over this region are small. However, these small values are not uncommon over land in the northern hemisphere. MODIS data also show the highest liquid water cloud fractions in the northern hemisphere over this area. Correlations between aerosols produced with models and observed cloud optical depths and a corresponding anti-correlation with effective radii suggest that aerosol indirect effects contribute to this feature (e.g., Chameides et al., 2002; Kawamoto et al., 2004). Aside from this area, the highest values of SW RF occur in coastal and low lying terrain areas of Antarctica

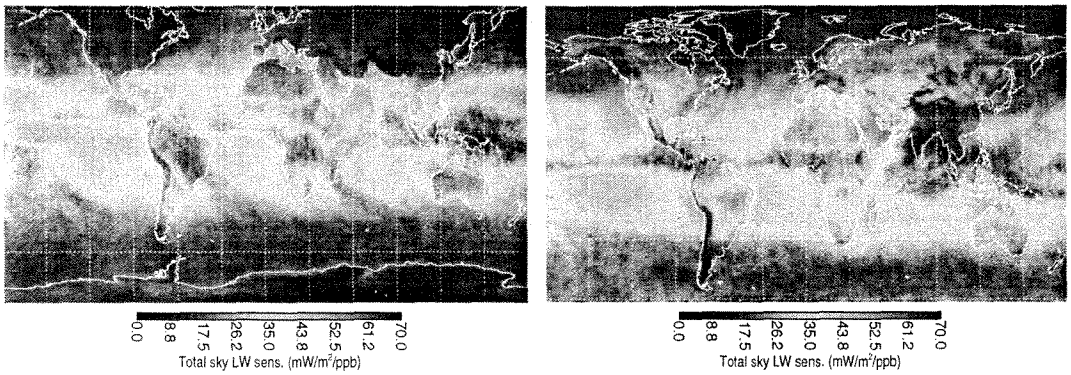

Fig. 6. Sensitivity of the LW RF to ozone mixing ratio for January (left) and July (right) 2005.

where the bright surface enhances the photon pathlength.

There is a large amount of SW RF over Greenland and arctic sea ice in July. There are also high values of SW RF in areas with persistent cloud cover and pollution outflow, such as off the east coast of Asia, both coasts of North America, and north of Europe. Despite the lack of cloudiness over the Sahara, there is considerable SW RF due to its relatively high surface albedo. Contributions to the SW RF from biomass burning can be seen near and off the west coasts of South America and Africa where cloud effects are significant.

Figure 8 shows the SW RF sensitivity similar to figure 6. Although the SW sensitivity is relatively high in the southern middle to high latitudes in January, the SW RF is low due to relatively low amounts of tropospheric O_3. In July, however, high sensitivity in the Arctic coupled with relatively high tropospheric O_3 produces a significant amount of SW RF.

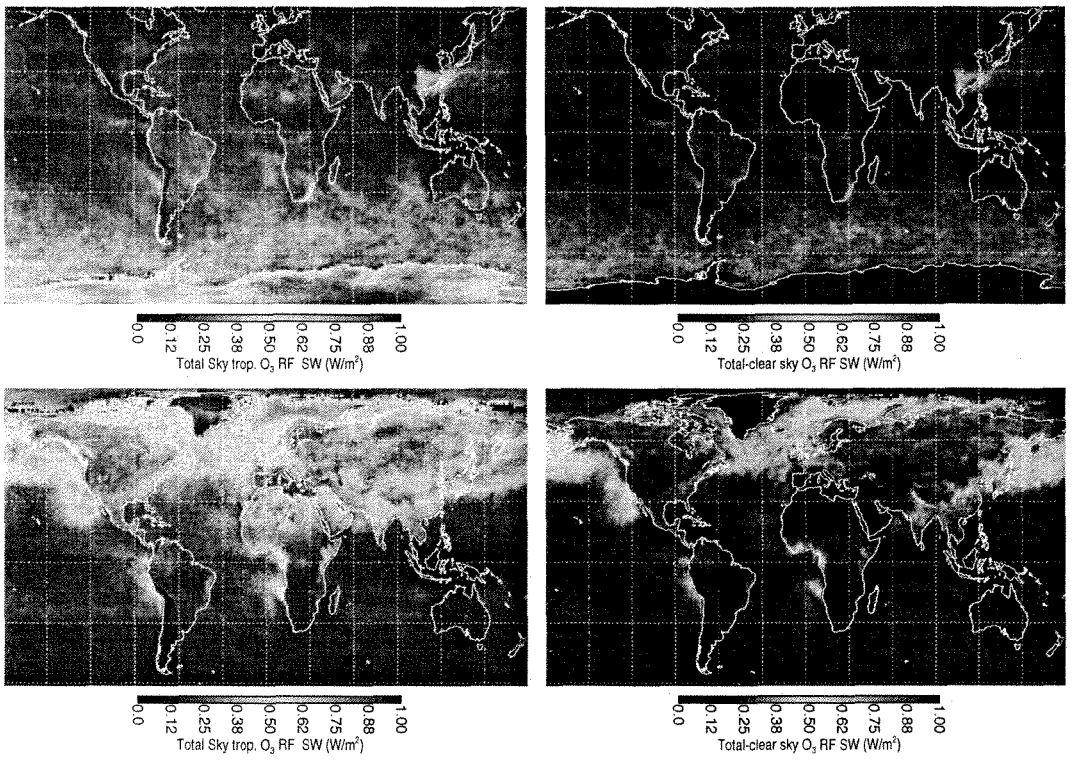

Fig. 7. Total-sky short-wave (SW) tropospheric O_3 RF in 2005: January (top left) and July (bottom left); Total minus clear-sky SW RF: January (top right) and July (bottom right).

4 Discussion

Global and zonal mean values of LW and SW RF and corresponding sensitivities are summarized in Table 1. Values of the net (LW+SW) RF and sensitivity are given in

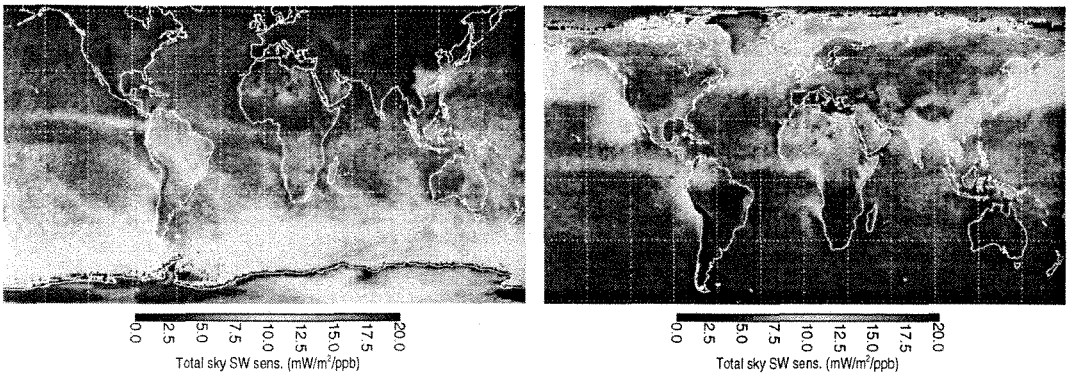

Fig. 8. Sensitivity of the SW RF to ozone mixing ratio for January (left) and July (right) 2005.

Table 2. A cosine latitude weighting is applied to calculate the mean values. On a global mean basis, the clouds reduce the LW RF by 25%, while they nearly double the SW RF. The reduction in the net RF is about 15%. However, as can be seen in table 2, there are large variations in cloud effects due to the partitioning between LW and SW that changes with solar zenith angle.

Our estimates of the present day tropospheric O_3 RF may be used to check the realism of various aspects of the anthropogenic tropospheric O_3 RF computed with CTM/GCMs. For example, our global-mean estimate of the ratio of the LW to net RF ($\sim$ 83%) is somewhat higher than that from models ($\sim$ 70-80%) (e.g., Hauglustaine et al., 2001, and references therein).

The most recent IPCC report provides an estimated value of radiative forcing at the tropopause (after stratospheric adjustment) due to anthropogenic tropospheric ozone of +0.35 (-0.1, +0.3) W/m^2 (Forster et al., 2007). This estimate is the median of the adjusted radiative forcing derived from an ensemble of CTMs/GCMs. The reported un-

Table 1. Computed LW/SW global and zonal mean tropospheric O_3 RF (W/m^2) and sensitivity ($(W/m^2/ppb)$ for 2005 with standard deviations in parentheses.

	LW RF total	LW RF total-clear	LW sens. total	SW RF total	SW RF total-clear	SW sens. total
Jan. 90°S-60°N	0.92(0.52)	-0.32(0.21)	24.9(12.7)	0.19(0.12)	0.09(0.08)	5.7(4.7)
Jan. 20°S-20°N	1.13(0.48)	-0.32(0.20)	33.5(9.4)	0.16(0.05)	0.06(0.04)	5.3(1.4)
Jan. 20°N-60°N	0.75(0.45)	-0.33(0.26)	17.5(10.2)	0.13(0.06)	0.06(0.05)	3.1(1.3)
Jan. 20°S-60°S	0.97(0.47)	-0.35(0.12)	25.1(10.2)	0.26(0.06)	0.15(0.07)	7.2(1.7)
Jan. 60°S-90°S	0.29(0.11)	-0.22(0.16)	9.9(3.5)	0.38(0.13)	0.12(0.12)	13.6(5.2)
July 60°S-90°N	1.19(0.55)	-0.36(0.22)	26.5(10.4)	0.24(0.22)	0.11(0.13)	5.2(3.9)
July 20°S-20°N	1.18(0.49)	-0.33(0.23)	31.7(9.2)	0.18(0.08)	0.08(0.06)	5.3(1.6)
July 20°N-60°N	1.58(0.61)	-0.42(0.25)	26.7(9.9)	0.38(0.14)	0.19(0.15)	6.5(2.3)
July 20°S-60°S	0.93(0.36)	-0.36(0.15)	22.7(7.7)	0.12(0.04)	0.05(0.02)	2.9(0.9)
July 60°N-90°N	0.77(0.24)	-0.33(0.18)	13.9(3.8)	0.52(0.25)	0.22(0.14)	9.6(5.2)

certainties arise from two sources: 1) The CTMs and GCMs themselves, including the imbedded radiative transfer codes, and 2) uncertainties in the estimated pre-industrial ozone levels.

In table 3, we compare several model-based RF estimates that have used observations as constraints. Note that some of these are older simulations and were not included in the most recent reported IPCC estimate. Mickley et al. (2001) adjusted the emissions of ozone precursors in their model to bring pre-industrial ozone concentrations into better agreement with surface observations over Europe from late nineteenth and early twentieth observations (7-10 ppb). These observations have a large uncertainty related to potential calibration problems (e.g., Volz and Kley, 1988; Pavelin et al., 1999). The resulting radiative forcing was significantly higher (0.72-0.80 W/m^2) than the typical range produced by standard model runs. This contributes to the large uncertainty in the positive direction in the current IPCC report.

Table 2. Computed net (LW+SW) global and zonal mean tropospheric O_3 RF (W/m^2) and sensitivity ($mW/m^2/ppb$) for 2005

	Net RF total	%LW RF	Net RF total-clear	% Net RF (total-clear)/clear	Net sens. total
Jan. 90°S-60°N	1.11	82.9	-0.23	-17.2	30.6
Jan. 20°S-20°N	1.29	87.6	-0.26	-16.8	38.8
Jan. 20°N-60°N	0.88	85.2	-0.27	-23.5	20.6
Jan. 20°S-60°S	1.23	78.9	-0.20	-14.0	32.3
Jan. 60°S-90°S	0.67	43.3	-0.10	-13.0	23.5
July 60°S-90°N	1.43	83.2	-0.25	-14.9	31.7
July 20°S-20°N	1.36	86.8	-0.25	-15.5	37.0
July 20°N-60°N	1.96	80.6	-0.23	-10.5	33.2
July 20°S-60°S	1.05	88.5	-0.31	-22.8	25.6
July 60°N-90°N	1.29	59.7	-0.11	-7.9	23.5

Kiehl et al. (1999) constrained their present-day tropospheric ozone estimates with satellite data. They used tropospheric columns from the residual approach of Fishman and Brackett (1997). In that work, the stratospheric column was derived from averages of several years of Stratospheric Aerosol and Gas Experiment (SAGE) occultation data and the total column was from the version 7 TOMS. This yielded data between 50°S and 50°N that were accurate to approximately 20% when compared with ozonesonde data. Model-generated cloud fractions were constrained such that the global mean cloud cover agreed with that from the International Satellite Cloud Climatology Project (ISCCP). They computed an instantaneous RF value of 1.55 W/m^2 assuming a preindustrial O_3 mixing ratio of 5 ppb at all tropospheric altitudes.

Berntsen et al. (1997) used cloud amounts, cloud levels, and optical depths from ISCCP. They similarly imposed observational constraints on present-day O_3 distributions using data from TOMS, SBUV, and SAGE (in the Reading model). They used a CTM to

Table 3. Computed net (LW+SW) tropospheric O_3 RF (W/m^2). The values are instantaneous (not adjusted) unless otherwise noted.

reference	RF	ozone, cloud data sources
IPCC*	0.35 (-1,+0.3)	model clouds RF is median of an ensemble of models
Kiehl et al. (1999)	1.55	model clouds constrained to ISCCP cloud amount present-day O_3 constrained with satellite data pre-industrial O_3 5 ppb
Mickley et al. (2001)	0.72-0.80	model clouds pre-industrial O_3 adjusted to uncertain surface observations
Berntsen et al. (1997, Reading)	0.35	ISCCP cloud properties present-day O_3 distributions constrained with satellite data absolute O_3 changes from CTM
Berntsen et al. (1997, OsloRad)	0.38	ISCCP cloud properties O_3 distributions from CTM
This work**	1.27	satellite-based clouds and O_3 anthropogenic + natural O_3 (pre-industrial O_3 0 ppb)

*Stratospheric-adjusted, not instantaneous

**January-July average, polar night region excluded

compute the absolute O_3 changes over the industrial era. They also computed the RF from pure CTM O_3 distributions (OsloRad). The resulting difference in instantaneous clear-sky LW RF (20%) indicates that uncertainty in the present-day O_3 distributions also contributes to the overall uncertainty in RF. Their computed RF, after stratospheric adjustment, is slightly below the IPCC median. It is roughly half that of the high values of Mickley et al. (2001) and roughly a quarter of the upper limits reported in Kiehl et al. (1999) and our study.

Our January-July average (1.27 W/m^2) is somewhat lower than the Kiehl et al. (1999) result, particularly considering that our RF was computed with respect to 0 ppb. However, it is well above the value of 0.8 W/m^2 from Mickley et al. (2001) that represents the highest model-based estimate of anthropogenic tropospheric O_3 RF.

Worden et al. (2008) computed the instantaneous clear-sky RF at the top of the atmosphere (TOA) from 985-1080 cm^{-1} due to O_3 between 200 and 500 hPa over ocean from 45°S to 45°N. They obtained a 2006 annual average TOA RF of 0.45 W/m^2 based on data from the NASA Aura Tropospheric Emission Spectrometer (TES). We similarly computed the clear-sky TOA RF for the same conditions except for the entire tropospheric column. Our January and July average was 0.95 W/m^2. This indicates that the RF due to tropospheric O_3 between 500 hPa and the surface and between 200 hPa and the tropopause is significant. Note that for these conditions, clouds decrease the clear-sky TOA RF by approximately 0.23 W/m^2 or 24%.

Table 4 summarizes reported estimates of the cloud impact on tropospheric O_3 RF. Roelofs (1999) demonstrated the importance of using instantaneous rather than monthly mean cloud properties, especially for shortwave RF calculations as noted in the table. The short-wave cloud effects are highly variable with our results falling in the middle of those reported earlier using either purely model-based clouds or clouds constrained by satellite data. We note that the treatment of cloud overlap varied in the model-based studies. The difference in the SW results appear to have be significantly influenced by the assumed surface albedo as Roelofs (1999) showed larger variations in the reported clear-sky RF from the different studies than in the total-sky. Similarly,

Table 4. Computed impact of clouds on tropospheric O_3 RF (not adjusted) (clear-sky - total-sky)/clear-sky$\times$100 (%)

reference	LW (%)	SW (%)	Net (%)	cloud source
Roelofs (1999, inst. clouds)	-24	125	-10	model
Roelofs (1999, avg. clouds)	-19	150	-2	model
Hauglustaine et al. (2001)	-18	50	-10	model
Berntsen et al. (1997, Reading)	-20	40	-13	ISCCP
Berntsen et al. (1997, OsloRad)	-29	33	-21	ISCCP
Haywood et al. (1998, inst. clouds)	-30	250	-17	model
Haywood et al. (1998, avg. clouds)	-31	150	-22	model
This work**	-24	87	-16	MODIS/OMI

**January-July average, polar night region excluded

there is a larger variation in the clear-sky LW RF than in the total-sky. This appears to be primarily due to differences in the O_3 distribution. Our LW and net cloud impacts fall in the middle of the dstribution of reported results.

We can compare our monthly tropospheric O_3 and RF with similar seasonal maps shown in Mickley et al. (1999, 2004) and Wong et al. (2004). In Mickley et al. (1999), the preindustrial ozone mixing ratio at 500 hPa displayed little longitudinal variability. We find many similar spatial and temporal features in the LW RF, but also some notable differences. Both models and satellite data show high tropospheric O_3 mixing ratios and RF in the southern hemisphere due to biomass burning and in the northern hemisphere middle latitudes in July. Our satellite-based estimates show high LW RF over Australia in January whereas the model results are somewhat lower. We also have a substantially larger area of low RF over the Pacific due to the low O_3 mixing ratios derived by the OMI/MLS residual technique. It also appears that we have lower relative amounts of RF in this area. Our approach also produces relatively lower amounts of LW RF in the Arctic during summer.

In the SW, the high RF over southeast Asia in January in our results is not present in Mickley et al. (1999), indicating that the cloudiness responsible for the high values is not present in their model. We find higher amounts of SW RF at middle latitudes relative to the Arctic than in Mickley et al. (1999) and Wong et al. (2004). This suggests that the models may not be producing enough SW RF in cloudy regions. This is particularly apparent in the north Atlantic and north Pacific as well as off the west coast of North America where there are persistent marine stratocumulus.

5 Conclusions

We have improved estimates of daily tropospheric O_3 mixing ratios in cloudy areas by using optical centroid cloud pressures (OCCP) from OMI. We derived column-mean mixing ratios that correspond to a thick tropospheric layer between the tropopause and an effective pressure that can be computed using the OMI cloud fraction and OCCP.

We have computed the present day radiative forcing from tropospheric O_3 using, to our knowledge, the most accurate daily global satellite data available to date consisting of several coincident datasets from the A-train. Our approach provides improved temporal and spatial coverage and a more detailed account of cloud effects than previous efforts that utilized satellite data exclusively. We note that it is important to have coincident retrievals of appropriate cloud properties and tropospheric ozone. In unpolluted oceanic areas (e.g., the remote Pacific), O_3 mixing ratios inside and above clouds can be very low, leading to low values of both LW and SW RF. However, in polluted regions, O_3 mixing ratios can be relatively large inside and above clouds. This can lead to significant amounts of LW and SW RF over low lying clouds and also large amounts of SW RF in convective clouds.

Appendix A Chou-Suarez radiative transfer code

In the SW CS code, the spectrum is divided into 8 bands in the ultraviolet (UV) and photosynthetically active (PAR) regions with a single ozone absorption coefficient and Rayleigh scattering coefficient in each band. There are 3 bands in the SW infrared where the k-distribution method is employed. Ozone absorption is accounted for in nine short-wave bands. The band-mean ozone transmission function was computed as the extraterrestrial solar flux-weighted mean; The UV and PAR regions were divided into 127 narrow bands of width $\sim 0.003 \mu$m with ozone absorption coefficients as given in WMO (1986). Similarly, a mean effective Rayleigh scattering coefficient was computed for ten of the bands. Differences between fluxes computed at high spectral-resolution and the parameterization were typically small ($< 2\%$) for ozone.

Reflection and transmission of cloud and aerosol layers are calculated using the δ-Eddington approximation, and fluxes are computed with a two-stream adding model. Spectral data provided by Fu (1996) for ice clouds and Tsay et al. (1989) for water clouds are used to derive an effective band-mean single scattering albedo, extinction coefficient, and asymmetry factor.

Thermal IR calculations in the LW are divided into eight bands. In order to optimize the algorithm for both speed and accuracy, Planck-weighted flux transmittances for gaseous absorption are computed using three different approaches, dependent on the absorber and band. The k-distribution method with linear pressure scaling is used for water vapor bands. Pre-computed transmittance tables based on two-parameter scaling are used to compute CO_2 and O_3 absorption in 15 and 9.6μm bands, respectively, as well as for the three strongest water vapor bands. Water vapor continuum absorption is similarly computed using a one parameter scaling approach. Differences between these parameterizations and line-by-line calculations were generally less than 1%, leading to errors much smaller than 1 W/m^2. O_3 absorption is computed only in the 9.6μm; Weaker absorption in the 14μm spectral region is not included.

For all LW calculations, we used the so-called "high" option the CS code, which

provides the highest degree of accuracy at increased computational cost. Calculations are performed in 36 fixed layers between 1000 and 0.01 hPa as specified in the GEOS-5 pressure level data. A smaller number of layers is used when the surface pressure is less than 1000 hPa.

The CS code was configured to accept profiles of cloud optical depth, effective radius, and cloud fraction separately for liquid and ice clouds. Although the code can also accept profiles of rain, this option was not exercised here. We describe how MODIS data are used with these inputs below. For LW calculations, we multiply the visible optical depth by empirical factors of 2.13 and 2.56 for ice and liquid, respectively, following Minnis et al. (1993) and Rossow and Schiffer (1999).

Although aerosols can be included in the CS code, we have not included their effects here. Non-absorbing aerosol will generally increase SW RF similar to the effect of clouds. Saharan dust absorbs in the 9.6μm band and can therefore decrease LW RF. Dust can also contaminate infrared temperature retrievals or radiance assimilation if not properly accounted for (e.g., Weaver et al., 2003).

We compared RF computed with the CS code in a clear-sky mid-latitude summer case with that from several other radiative transfer (RT) codes examined in the intercomparison of Shine et al. (1994) by using their supplied profile information. The CS-computed SW tropospheric O_3 RF was 0.0184W/m^2 which is also somewhat lower than the ensemble mean (0.022W/m^2), but well within the range of results (0.017-0.031W/m^2, $\sigma = 0.0046$W/m^2). The LW O_3 RF from CS (0.140 W/m^2) was approximately 10% less than the mean of the ensemble of RT calculations for the case where tropospheric ozone was perturbed. Note that some of the RT models include the 14μm band while others (including CS) do not. This band contributes about 2% of the forcing in this case (Shine et al., 1994).

Differences in the LW O_3 RF may occur due to differences in the assumed O_3 absorption coefficients as well as differences in the specification of the water vapor continuum which significantly affects the computed top-of-the-atmosphere (TOA) radiances and fluxes in the 9.6μm band (Joiner et al., 1998). CS uses the version CKD2.3 water

vapor continuum model of Clough et al. (1989).

Appendix B Sensitivity studies

Here, we perform a series of sensitivity calculations on a single day (01 July 2005).

B1 Sensitivity to cloud optical properties

In the first experiment, we found very little sensitivity of the tropospheric O_3 RF to the input cloud phase which determines the parameterized values of the single scattering albedo, extinction coefficient, and asymmetry factor. We similarly found little sensitivity to the cloud effective radius. Therefore, for all subsequent calculations we use the MODIS daily gridbox mean effective radius rather than averaging over its histogram or joint histogram with cloud optical thickness. If there was a successful liquid water cloud retrieval within a gridbox, regardless of whether or not there was a successful ice cloud retrieval, we use the mean effective radius of the liquid water cloud retrievals and specify the phase as water. Otherwise, we assume the cloud to be ice and use the effective radius of the ice cloud retrievals.

Our RF calculations, as expected, show a non-linear dependence on the cloud optical thickness. We examined the differences in RF computed with gridbox the mean cloud optical thickness ($\overline{\tau}$) versus calculations performed over the distribution of cloud optical thicknesses and then appropriately averaged using the reported histograms (full τ). Although Oreopoulos et al. (2007) have shown that the full τ approach is more appropriate for calculations of cloud radiative forcing, here the differences for tropospheric O_3 RF were small (of the order of 0.01 W/m^2 or less). Mean differences over the latitude range 45°S to 45°N are small (< 0.003 W/m^2 with $\sigma < 0.025$ W/m^2) in both the LW and diurnally-averaged SW. All results shown here use the $\overline{\tau}$ formulation.

B2 Sensitivity to cloud vertical structure

We compared two different methods of vertically distributing the total cloud optical thickness: 1) Cloud distributed over a 100 hPa layer centered at the lesser of the OMI optical centroid cloud pressure (OCCP) or the surface pressure minus 50 hPa 2) Cloud distributed over a 100 hPa layer with the top specified as the MODIS cloud-top pressure. As expected, differences in both the LW and SW have spatial patterns similar to the differences between the OMI OCCP and the MODIS cloud-top pressure shown in figure 3 with larger magnitudes in areas of high O_3 mixing ratios.

There are differences in the SW local RF of $\sim$50% in regions of heavy convective cloud cover where the ozone mixing ratios are high. Comparable but slightly larger differences (in terms of percent) occur in the LW RF. Averaged globally, RF is $\sim$8% and 12% less when using the cloud-top pressure as compared with the OCCP for the LW and SW, respectively.

Here, we use the MODIS cloud top pressure for LW RF calculations. In the LW, TOA radiances saturate as the visible optical depth reaches values of $\sim$4. For deep convective clouds, the appropriate pressure would be close to the cloud top pressure (see e.g., Ziemke et al., 2008). However, the use of the cloud top pressure for LW RF calculations will produce an underestimate if the optical depth of the upper cloud deck is less than about 4.

We use the OMI OCCP for SW RF calculations as it more accurately accounts for O_3 absorption in cloudy conditions (Ziemke et al., 2008). Note that enhanced SW absorption can occur in the presence of multiple cloud layers, particularly at low solar zenith angles and when the optical depth of the upper cloud deck is less than about 10. The use of the OMI OCCP accounts for this effect because the retrieved cloud pressure increases when enhanced absorption/scattering occurs (Vasilkov et al., 2008), though there will likely be a small residual error in a full flux calculation because the cloud pressure was derived at a particular viewing geometry.

B3 Sensitivity to tropopause definition

The tropopause pressure affects the calculation of the tropospheric mixing ratio from Eq. 2 in two ways: The denominator (the pressure difference between the surface/cloud and tropopause) is larger for the lapse-rate tropopause and results in lower mixing ratios. However, the residual tropospheric column amount in the numerator will be larger for the higher lapse-rate tropopause. The latter effect dominates as derived column-mean mixing ratios are generally higher with the lapse rate definition.

The SW O_3 RF depends primarily on the tropospheric column amount, which is nearly always larger for the lapse-rate tropopause definition. The global mean difference in computed SW RF using the two tropopause definitions (lapse-rate - PV) was 6% with maximum differences of $\sim$ 70-90% in narrow regions where the tropopause gradient is steep.

The LW forcing is more sensitive to ozone and temperature profiles in the vicinity of the tropopause where the gradient of the net flux is large. The differences in LW O_3 RF resulting from different tropopause definitions are both positive and negative. Similar to the SW results, the global mean LW difference is $\sim$6% with local differences in the range $\sim \pm$70-90%.

Acknowledgements. The authors thank the OMI, MLS, and MODIS science teams for the processing, validation, and distribution of data sets used here. The lead author acknowledges helpful discussions with A. da Silva. This material is based upon work supported by NASA under agreement NNG06HX18C issued through the Science Mission Directorate for the Aura Science Team. Lazaros Oreopoulos gratefully acknowledges support for this work by the US Department of Energy, Office of Science, Office of Biological and Environmental Research, Environmental Sciences Division as part of the ARM program under grant DE-FG02-07ER64354. Work at the Jet Propulsion Laboratory, California Institute of Technology was performed under contract with NASA.

References

Berntsen, T.K., Isaksen, I.S.A., Myhre, G., Fuglestvedt, J.S., Stordal, F. T., Larsen, A., Freckleton, R.S., Shine, K.P.: Effects of anthropogenic emissions on tropospheric ozone and its radiative forcing, J. Geophys. Res., 102, 28101–28126, 1997.

Bhartia, P.K., Wellemeyer, C. W.: TOMS-V8 total O_3 Algorithm, OMI Algorithm Theoretical Basis Document, vol. 2, ed. by P. K. Bhartia, Greenbelt, Md, http://toms.gsfc.nasa.gov/version8/v8toms_atbd.pdf, 2002.

Chameides, W. L., Luo, C., Saylor, R., Streets, D., Huang, Y., Bergin, M., Giorgi, F.: Correlation between model-calculated anthropogenic aerosols and satellite-derived cloud optical depths: Indication of indirect effect?, J. Geophys. Res., 107, doi:10.1029/2000JD000208, 2002.

Chou, M.-D., Suarez, M. J.: An efficient thermal infrared radiation parameterization for use in general circulation models, NASA Tech. Memo 104606, Vol. 3, 85 pp., 1994.

Chou, M.-D., Suarez, M. J.: A solar radiation parameterization for atmospheric studies, NASA Tech. Memo 104606, Vol. 15, 40pp., 2002.

Chou, M.-D., M. J. Suarez, X.-A. Liang, M. M.-H. Yan, A thermal infrared radiation parameterization for atmospheric studies, NASA Tech. Memo 104606, Vol. 19, 85 pp., 2003.

Clough, S. A., Kneizys, F. X., Davies, R. W.: Line shape and the water vapor continuum, Atmos. Res., 23, 229–241, 1989.

Dessler, A.: The Chemistry and Physics of the Stratosphere, Elsevier, New York, 214 pp., 2005.

Fishman, J., Brackett, V.: The climatological distribution of tropospheric ozone derived from satellite measurements using version 7 Total Ozone Mapping Spectrometer and Stratospheric Aerosol and Gas Experiment data sets, J. Geophys. Res., 102, 19275-19278, 1997.

Folkins, I., Braun, C., Thompson, A. M., Witte, J.: Tropical ozone as an indicator of deep convection, J. Geophys. Res., 107, doi:10.1029/2001JD001178, 2002.

Forster, P., Johnson, C., Law, K., Pyle, J., Shine, K.: Further Estimates of Radiative Forcing Due to Tropospheric Ozone Changes, Geophys. Res. Let., 23, 3321-3324, 1996.

Forster, P. et al.: in The Fourth Assessment Report of the Intergovernmental Panel on Climate Change, ed. Solomon, S. et al.., Cambridge Univ. Press, Cambridge, 2007.

Froidevaux, L., et al.: Validation of Aura Microwave Limb Sounder stratospheric ozone measurements, J. Geophys. Res., 113, D15S20, doi:10.1029/2007JD008771, 2008.

Fu, Q.: An accurate parameterization of the solar radiative properties of cirrus clouds for climate models, J. Clim., 9, 2058–2082, 1996.

Gauss, M. et al..: Radiative forcing since preindustrial times due to ozone change in the troposphere and the lower stratosphere, Atmos. Chem. Phys., 6, 575599, 2006.

Hauglustaine, D. A., Brasseur, G. P.: Evolution of tropospheric ozone under anthropogenic activities and associated radiative forcing of climate, J. Geophys. Res., 106, 32337–32360, 2001.

Haywood, J. M., Schwarzkopf, M. D., Ramaswamy, V.: Estimates of radiative forcing due to modeled increases in tropospheric ozone, J. Geophys. Res., 103, 16,99917,007, 1998.

Jin, Z., Charlock, T., Smith, W., Rutledge, K.: A parameterization of ocean surface albedo, Geophys. Res. Let., 31, L22301, doi:10.1029/2004GL021180, 2004.

Joiner, J., Lee, H. T., Strow, L. L., Bhartia, P. K., Hannon, S., Miller, J., Rokke, L.: Radiative transfer in the 9.6 micron HIRS ozone channel using collocated SBUV-determined ozone abundances, J. Geophys. Res., 103, 19,213-19,229, 1998.

Joiner, J., Vasilkov, A. P., Flittner, D. E., Gleason, J. F., Bhartia, P. K.: Retrieval of cloud pressure and oceanic chlorophyll content using Raman scattering in GOME ultraviolet spectra, J. Geophys. Res., 109, D01109, doi:10.1029/2003JD003698, 2004.

Joiner, J., Vasilkov, A. P.: First results from the OMI Rotational Raman Scattering Cloud Pressure Algorithm, IEEE Trans. Geosci. Rem. Sens., 44, 1272-1282, 2006.

Joiner, J., Vasilkov, A. P., Yang, K., Bhartia, P. K.: Total column ozone over hurricanes from the Ozone Monitoring Instrument, Geophys. Res. Let., 33, L06807, doi:10.1029/2005GL0255922006, 2006.

Kawamoto, K., Hayasaka, T., Nakajima, T., Streets, D., Woo, J.-H.: Examining the aerosol indirect effect over China using an SO_2 emission inventory, Atmos. Res., 72, 353–363, 2004.

Kiehl, J. T., Schneider, T. L., Portmann, R. W., Solomon, S.: Climate forcing due to tropospheric and stratospheric ozone, J. Geophys. Res., 104, 31239-31254, 1999.

Kley, D., Crutzen, P. J., Smit, H. G. J., et al..: Observations of near-zero ozone concentrations over the convective Pacific: Effects on air chemistry, Science, 274, 230-233, 1996.

Kroon, M., Petropavlovskikh, I., Shetter, R. E., Hall, S., Ullmann, K., Veefkind, J. P., McPeters, R. D., Browell, E. V., Levelt, P.: OMI Total Ozone Column Validation with Aura-AVE CAFS Observations, J. Geophys. Res., doi:10.1029/2007JD008795, 2008.

Kroon, M., Veefkind, J. P., Sneep, M., McPeters, R. D., Bhartia, P. K., Levelt, P. F.: Comparing OMI-TOMS and OMI-DOAS total ozone column data, J. Geophys. Res., doi:10.1029/2007JD008798, 2008.

Levelt, P. F., et al.., The Ozone Monitoring Instrument, IEEE Trans. Geophys. Remote Sens.,

44, 1093-1101, 2006.
Li, Q. B., et al.: A tropospheric ozone maximum over the Middle East, Geophys. Res. Lett., 28, 3235-3238, 2001.
Livesey, N. J., et al., Validation of Aura Microwave Limb Sounder O_3 and CO observations in the upper troposphere and lower stratosphere, J. Geophys. Res., 113, D15S02, doi:10.1029/2007JD008805, 2008.
Lucht, W., Schaaf, C. B., Strahler, A. H.: An Algorithm for the retrieval of albedo from space using semiempirical BRDF models, IEEE Trans. Geosci. Remote Sens., 38, 977-998, 2000.
McPeters, R. D., Kroon, M., Labow, G. J., Brinksma, E., Balis, D., Petropavlovskikh, I., Veefkind, J. P., Bhartia, P. K., Levelt, P. F.: Validation of the Aura Ozone Monitoring Instrument Total Column Ozone Product, J. Geophys. Res., doi:10.1029/2007JD008802, 2008.
Menzel, W. P., Wylie, D. P., Strabala, K. I.: Seasonal and diurnal changes in cirrus clouds as seen in four years of observations with the VAS, J. Appl. Meteorol., 31, 370–385, 1992.
Mickley, L. J., Murti, P. P., Jacob, D. J., Logan, J. A., Koch, D. M., Rind, D.H.: Radiative forcing from tropospheric ozone calculated with a unified chemistry-climate model, J. Geophys. Res., 104, 30153–30172, 1999.
Mickley, L. J., Jacob, D. J., Rind, D.H.: Uncertainty in preindustrial abundance of tropospheric ozone: Implications for radiative forcing calculations, J. Geophys. Res., 106, 3389–3399, 2001.
Mickley, L. J., Jacob, D. J., Field, B. D., Rind, D.H.:Climate response to the increase in tropospheric ozone since preindustrial times: A comparison between ozone and equivalent CO2 forcings, J. Geophys. Res., 109, D05106, doi:10.1029/2003JD003653, 2004.
Minnis, P., Liou, K.-N., Takano, Y.: Inference of cirrus cloud properties using satellite-observed visible and infrared radiances. Part I: Parameterization of radiance field. J. Atmos. Sci., 50, 1279–1304, 1993.
Nolin, A., Armstrong, R. L., Maslanik, J.: Near Real-Time SSM/I EASE-Grid Daily Global Ice Concentration and Snow Extent, January to March 2004 (updated daily). Boulder, CO, USA: National Snow and Ice Data Center. Digital media, 1998.
Oreopoulos, L., Cahalan, R., Platnick, S.: The plane-parallel albedo bias of liquid clouds from MODIS observations. J. Climate, 20, 5114-5125, 2007.
Pavelin E. G., Johnson C. E., Rughooputh S., Toumi R., Evaluation of pre-industrial surface ozone measurements made using Schonbein's method, Atmos. Env., 33, 919–929, 1999.
Petropavlovskikh, I., Froidevaux, L., Shetter, R., Hall, S., Ullmann, K., Bhartia, P. K., Kroon,

M., Levelt, P. F.: In-flight validation of Aura MLS ozone with CAFS partial ozone columns, J. Geophys. Res., 113, doi:10.1029/2007JD008690, 2008.
Platnick, S., King, M. D., Ackerman, S. A., Menzel, W. P., Baum, B. A., Ridi, J. C., Frey, R. A.: The MODIS cloud products: algorithms and examples from Terra, IEEE Trans. Geosci. Rem. Sens., 41, 459-473, 2003.
Portmann, R. W., Solomon, S., Fishman, J., Olson, J. R., Kiehl, J. T., Briegleb, B.: Radiative forcing of the Earth's climate system due to tropical tropospheric ozone production, J. Geophys. Res., 102, 9409–9417, 1997.
Rienecker, M. M., et al.: The GEOS-5 data assimilation system - Documentation of versions 5.0.1, 5.1.0, and 5.2.0. NASA Tech. Memo. 2007-104606, vol. 27, M. J. Suarez, Editor., 2007.
Roelofs, G.-J.: Radiative Forcing by Tropospheric Ozone: Impact of Cloud Representation, Geophys. Res. Lett., 26, 467-470, 1999.
Rossow, W. B., Schiffer, R. A.: Advances in understanding clouds from ISCCP, Bull. Amer. Meteorol. Soc., 80, 2261–2287, 1999.
Rozanov, V. V., Kokhanovsky, A. A., Burrows, J. P.: The determination of cloud altitudes using GOME reflectance spectra: Multilayered cloud systems, IEEE Trans. Geosci. Rem. Sens., 42, 1009-1017, 2004.
Schoeberl, M. R., et al.: A trajectory-based estimate of the tropospheric ozone column using the residual method, J. Geophys. Res., 112, D24S49, doi:10.1029/2007JD008773, 2007.
Shine, K., Briegleb, B. P., Grossman, A. S., Hauglustaine, D., Mao, H., Ramaswamy, V., Schwarzkopf, M. D., Van Dorland, R., Wang, W.-C.: Radiative forcing due to changes in ozone: a comparison of different codes, In Atmospheric Ozone as a Climate Gas, Ed. W.-C. Wang and I. S. A. Isaksen, NASA ASI Series I: Global Environmental Change, Vol. 32, Springer-Verlag, Berlin, 373–396, 1994.
Sneep, M., De Haan, J., Stammes, P., Wang, P., Vanbauce, C., Joiner, J., Vasilkov, A. P., Levelt, P. F.: Three way comparison between OMI/Aura and POLDER/PARASOL cloud pressure products, J. Geophys. Res., doi:10.1029/2007JD008694, 2008.
Solomon, S., Thompson, D. W. J., Portmann, R. W., Oltmans, S. J., Thompson, A. M.: On the distribution of and variability of ozone in the tropical upper troposphere: Implications for tropical deep convection and chemical-dynamical coupling, Geophys. Res. Let., 32, L23813, doi:10.1029/2005GL024323, 2005.
Stephens, G. L., et al.: The CloudSat mission and the A-Train: A new dimension of space-

based observations of clouds and precipitation. Bull. Amer. Meteor. Soc., 83, 1771-1790, 2002.
Tsay, S. C., Stamnes, K., Jayaweera, K.: Radiative energy balance in the cloudy and hazy Arctic, J. Atmos. Sci., 46, 1002–1018, 1989.
Vasilkov, A. P., Joiner, J., Spurr, R., Bhartia, P. K., Levelt, P. F., Stephens, G.: Evaluation of the OMI cloud pressures derived from rotational Raman scattering by comparisons with other satellite data and radiative transfer simulations, J. Geophys. Res., 113, D15S19, doi:10.1029/2007JD008689, 2008.
Vasilkov, A. P., Joiner, J., Yang, K., Bhartia, P. K.: Improving total column ozone retrievals by using cloud pressures derived from Raman scattering in the UV, Geophys. Res. Let., 31, L20109, doi:10.1029/2004GL020603, 2004.
Volz, A. and Kley, D.: Evaluation of the Montsouris series of ozone measurements made in the nineteenth century, Nature, 332, 240-242, 1988.
World Meteorological Organization: Atmospheric ozone, global ozone research and monitoring project, vol. I, Report No. 16, 392 pp., 1986.
Weaver, C. J., Joiner, J., Ginoux, P.: Mineral aerosol contamination of TOVS temperature and moisture retrievals. J. Geophys. Res., 108, #4246, doi:10.1029/2002JD002571, 2003.
Wilber, A. C., Kratz, D. P., Gupta, S. K.: Surface emissivity maps for use in satellite retrievals of longwave radiation. NASA Tech. Pub. 1999-209362, 30 pp., http://www.sti.nasa.gov, Hanover, MD, USA, 1999.
Wong, S., Wang, W.-C., Isaksen, I. S. A., Berntsen, T. K., Sundet, J. K.: A global climate-chemistry model study of present-day tropospheric chemistry and radiative forcing from changes in tropospheric O3 since the preindustrial period, J. Geophys. Res., 109, D11309, doi:10.1029/2003JD003998, 2004.
Worden, H. M., Bowman, K. W., Worden, J. R., Eldering, A., Beer, R.: Satellite measurements of the clear-sky greenhouse effect from tropospheric ozone, Nature Geosci., 1, 305–308, 2008.
Ziemke, J. R., Chandra, S., Duncan, B. N., Froidevaux, L., Bhartia, P. K., Levelt, P. F., Waters, J. W.: Tropospheric ozone determined from Aura OMI and MLS: Evaluation of measurements and comparison with the Global Modeling Initiative's Chemical Transport Model, J. Geophys. Res., 111, D19303, doi:10.1029/2006JD007089, 2006.
Ziemke, J. R., Joiner, J., Chandra, S., Bhartia, P. K., Vasilkov, A. P., Haffner, D., Yang, K., Schoeberl, M. R., Froidevaux, L., Levelt, P. F.: Ozone mixing ratios inside tropical deep

convective clouds from OMI satellite measurements, Atmos. Chem. Phys. Disc., 8, 16381–16407, 2008.